Hyperspectral phase imaging based on denoising in complex-valued eigensubspace

Igor Shevkunov [a,d,*], Vladimir Katkovnik [a], Daniel Claus [b], Giancarlo Pedrini [c], Nikolay V. Petrov [d], Karen Egiazarian [a]

[a] *Tampere University, Faculty of Information Technology and Communication Sciences, Tampere, Finland*
[b] *Institut für Lasertechnologien in der Medizin und Messtechnik, HelmholtzstraÃß 12, Ulm 89081, Germany*
[c] *Institut für Technische Optik (ITO), Universität Stuttgart, Pfaffenwaldring 9, Stuttgart 70569, Germany*
[d] *ITMO University, Department of Photonics and Optical Information Technology, St. Petersburg, Russia*

ARTICLE INFO

ABSTRACT

A novel algorithm for reconstruction of hyperspectral 3D complex domain images (phase/amplitude) from noisy complex domain observations has been developed and studied. This algorithm starts from the SVD (singular value decomposition) analysis of the observed complex-valued data and looks for the optimal low dimension eigenspace. These eigenspace images are processed based on special non-local block-matching complex domain filters. The accuracy and quantitative advantage of the new algorithm for phase and amplitude imaging are demonstrated in simulation tests and in processing of the experimental data. It is shown that the algorithm is effective and provides reliable results even for highly noisy data.

1. Introduction

Hyperspectral imaging (HSI) enables the collection and processing of data from a large range of the electromagnetic spectrum. Its main applications are in high-quality and contrast imaging [1], chemical material identification [2], or process detection [3]. HSI retrieves information from images obtained across a wide spectral range and hundreds to thousands of spectral channels. Conventionally, these images are two-dimensional 2D and stacked together in 3D cubes, where the first two coordinates are spatial (x, y) and the third one is for the spectral channel, which is usually represented by the wavelength λ.

In recent years, coherent diffractive imaging (CDI) has enabled vast progress in high-resolution microscopy [4–6]. The central challenge in CDI is to acquire knowledge of the phase of the recorded field. Performing a direct measurement of the phase typically does come at the cost of increased measurement complexity. The main examples of such approaches are spectrally resolved interferometry [7–9] and Fourier transform holography [10–12] or Hyperspectral Digital Holography (HSDH) [9,13,14]. In these methods, the interference between a reference wave and a diffraction pattern is recorded and the observations, as well as the results, have a form of 3D hyperspectral cubes with complex-valued variables specified by both amplitude and phase. Similarly, 3D complex domain variables are appeared in close but different optical setups

where there are no reference beams. Spectrally resolved phase retrieval algorithms are used in these setups [15,16].

It seems, that HSDH is originated from the work of Itoh et al. [17] where the interferometric measurement of the three-dimensional Fourier-image of the diffusely illuminated and self-irradiated thermal objects was demonstrated for the first time for visible and near-infrared spectral ranges, correspondingly. A typical HSDH setup in these frequency ranges is based on a Fourier-transform spectrometer [18], where instead of a single-pixel detector a multi-pixel sensor (camera) used for the wavefront intensity registration. Later similar HSDH techniques have been developed for broadband terahertz pulses [19,20] and even for dissipated radiation for unmodified wireless devices [21].

As an advantage, HSDH recovers not only spectrally resolved intensity (amplitude) information, as in the conventional HSI, but also spectrally resolved phase information. For HSI it opens a new dimension of investigations with the possibility to recover information about height/thickness/relief and refractive indexes of complex-valued objects [22–24]. In HSDH, 3D data cubes are complex-valued, i.e. each of the 2D images for each wavelength is complex-valued having 2D phase and amplitude images. An important point here is that these cubes are obtained from indirect observations as solutions of ill-posed inverse problems. The latter leads to a serious amplification of all sorts of disturbances, in particular, measurement noises, in the resulting hyperspectral cubes.

Besides, due to the high spectral resolution, the energy obtained by sensors is separated between many narrow wavebands and limited in each band.

Narrowing the subject matter to the visible frequency range, it should be noted that radiation sources used in HSDH, as a rule, a less directed and weak. Additional, during the propagation through the optical setup the spectral content of the radiation could suffer from various losses associated with inhomogeneous spectral absorption, chromatic aberrations due to the presence of optical elements with a dispersion of the refractive index.

Due to all these limitations, HSI can be very sensitive to noise as well as to various nonidealities of optical systems. It is important especially when the hyperspectral sensor is not electronically stable, and the corruption of the electronic charge can affect the spectral value collection easily, especially in low-intensity illuminations that usually occur at the edges of the spectral range used [25]. Thus, the problem of noise is one of the significant obstacles to the development of these techniques.

For noise suppression, the averaging by the sample mean along the wavelength dimension is used routinely [20–22,26,27], but it may result in oversmoothing of the true signal with averaging over a large range of wavelengths. Development and application of more sophisticated algorithms for separate wavelength filtering of phase and amplitude appeared as a more efficient tool [28].

In this paper, we present a novel advanced algorithm for denoising of complex-domain hyperspectral (HS) data applicable for the multiple optical setups mentioned above providing final or intermediate results in the form of the complex-valued HS cubes.

The proposed algorithm preliminary estimates the complex-valued signal and noise correlation matrices and then selects a small-sized subset of the singular value decomposition (SVD) eigenvectors that best represents the signal subspace in the least squared error sense. The 2D complex-domain filtering is applied for denoising of this small number of eigenimages. The filtered eigenimages are used for reconstruction of the wavefield for all wavelengths. We show that visually and numerical accuracy, evaluated in terms of the relative root-mean-square error (RRMSE), the algorithm enables significantly better performance in comparison with the alternative modern techniques and the sliding window spectral averaging. The algorithm works successfully even with HS data characterized by the extremely small signal-to-noise ratio (SNR).

The algorithm presented in this paper is an essential modification of the algorithm presented in our conference paper [29]. The principal difference of this novel algorithm concerns a sliding window estimation when the original observation cube is partitioned on subcubes of smaller sizes. It is shown that this procedure results in valuable accuracy improvement as compared with the use of all observation slices simultaneously in [29]. This paper involves substantially more analytical, simulation and experimental development. In the developed Complex-domain Cube Filter (CCF), we apply the complex-domain block-matching 3D filter with Winner filtering (ImRe-BM3D WI) [30] for eigenimage denoising, contrary to it, a more simple and less effective filter was used for similar denoising in [29].

Technically, the algorithm is designed as a denoiser. The sparsity concept which is at the roots of the algorithm assumes a search for similar patches of images, then combine them and process together. These procedures result in some kind of robustness of the algorithm with respect to disturbances of nature different from standard additive noise, the model used in the algorithm design. In particular, the algorithm allows to produce good results for phase imaging for areas of slices of HS cube with very low amplitude values provided that there are slices with similar phase patches and stronger amplitude values. Thus, the developed algorithm is not restricted to noise filtering and can be treated as a more general instrument targeted for image reconstruction from various disturbances.

The paper is organized as follows. Section 2 describes a problem formulation and assumptions needed for its solution. In Section 3 the proposed denoising algorithm and its framework are presented. In Section 4 we present simulation experiments for algorithm parameters selection (Section 4.1), for validating filtering results and comparison with alternative filtering techniques on different objects (Section 4.2). The phase imaging results for HS data, that were obtained in HSDH experiments are discussed in Section 5. Final conclusions are in Section 6.

2. Problem formulation

Let $U(x, y, \lambda) \subset \mathbb{C}^{N \times M}$ be a slice of the complex-valued HS cube of the size $N \times M$ on (x, y) provided a fixed wavelength λ, and $Q_\Lambda(x, y) = \{U(x, y, \lambda), \lambda \subset \Lambda\}$, $Q_\Lambda \subset \mathbb{C}^{N \times M \times L_\Lambda}$, be a whole cube composed of a set of the wavelengths Λ with the number of individual wavelengths L_Λ. Thus, the total size of the cube is $N \times M \times L_\Lambda$ pixels.

The lines of $Q_\Lambda(x, y)$ contain L_Λ spectral observations corresponding to the scene with coordinates (x, y). Then, the observations of the hyperspectral denoising problem under the additive noise assumption may be written as:

$$Z_\Lambda(x, y) = Q_\Lambda(x, y) + \varepsilon_\Lambda(x, y), \tag{1}$$

where Z_Λ, Q_Λ, $\varepsilon_\Lambda \subset \mathbb{C}^{N \times M \times L_\Lambda}$ represent the recorded noisy HS data, clean HS data and additive noise, respectively. Spatial coordinates (x, y) are integer numbers belonging to ranges $[1: N]$ and $[1: M]$, respectively. Accordingly to the notation for the clean image, the noisy cube can be represented as $Z_\Lambda(x, y) = \{Z(x, y, \lambda), \lambda \in \Lambda\}$, $Z_\Lambda \subset \mathbb{C}^{N \times M \times L_\Lambda}$ with the slices $Z(x, y, \lambda)$.

The denoising problem is formulated as reconstruction of unknown $Q_\Lambda(x, y)$ from given $Z_\Lambda(x, y)$. The properties of the clean HS $Q_\Lambda(x, y)$ and the noise $\varepsilon_\Lambda(x, y)$ are essential for the algorithm development.

The following three assumptions are basic hereafter [31].

1. *Similarity* of the HS slices $U(x, y, \lambda)$ for nearby wavelengths λ. This similarity follows from the fact that on many occasions $U(x, y, \lambda)$ are slowly varying functions of λ, as it for instance for the phase delays due to propagation of hyperspectral light through an object of varying thickness. It follows from this similarity that the spectral lines of $Q_\Lambda(x, y)$ of the length L_Λ live in a k-dimensional subspace with $k \ll L_\Lambda$. Therefore, there is a linear transform E reducing the size of the cube $Q_\Lambda(x, y)$ to the cube of the smaller size. Following [31], we herein term the images associated with this k-dimensional subspace as *eigenimages*. A smaller size of this subspace automatically means a potential to improve the HS denoising being produced in this subspace. The sliding window algorithm developed in this paper is applicable in the scenario of piece-wise slowly varying slices $U(x, y, \lambda)$, see Section 4.2.2.

2. *Sparsity* of HS images $U(x, y, \lambda)$ as functions of (x, y). According to the definition, the sparsity means that there exist bases such that $U(x, y, \lambda)$ can be represented with a small number of items of these bases. This assumption is not restrictive in any practical situation as it concerns the algorithms for data processing looking for (or designing as it is in this paper) these bases and these bases are not applied to whole size $(N \times M)$ image-slices but to their small patches (often 8×8). The sparsity is one of the natural and fundamental assumptions for the design of modern image processing algorithms. The sparsity for complex-valued images is quite different from the standard formulation of this concept introduced for real-valued signals. The complex-valued variables can be defined by any of the two pairs: amplitude/phase and real/imaginary values and elements of these pairs are usually correlated [27,30].

3. The *noise* $\varepsilon_\Lambda(x, y)$ is zero mean circular complex-valued Gaussian with diagonal correlation matrix $L_\Lambda \times L_\Lambda$, i.e real and imaginary parts are uncorrelated and have the same Gaussian distributions.

Clean image subspace identification is a crucial first step in the developed algorithm. The signal and noise correlation matrices are estimated and then used to select the subset of eigenvectors that best represents the signal subspace in the least mean squared error sense.

3. Proposed algorithm

The following algorithmic techniques are the foundation of the proposed algorithm: A) Separate denoising of each slice of HS cube, i.e. slice-by-slice filtering; B) Joint simultaneous filtering of all slices in HS cube; C) Sliding window filtering of HS cube with joint slice filtering in each window.

The concept of the complex domain sparsity is exploited here in two different modes which we call 'local' and 'global'. The local sparsity is what is applied to the level of image patches in slice-by-slice (filtering A). The global sparsity appears in a joint analysis of HS slices when we use SVD applied to whole HS cube (filtering B) or to its fragments in sliding window filtering of HS cube (filtering C).

3.1. Separate slice denoising

The algorithms of this group filter the images of the HS cube for the each wavelength separately with the result which can be shown as

$$\hat{U}(x, y, \lambda) = CDBM3D\{Z(x, y, \lambda)\}, \ \lambda \in \Lambda, \tag{2}$$

where $CDBM3D$ is the abbreviation for Complex Domain Block-Matching 3D filter and $\hat{U}(x, y, \lambda)$ is an estimate of the clean unknown wavefront $U(x, y, \lambda)$.

The complex domain BM3D algorithm is originated in [32]. This concept has been generalized and a wide class of the complex domain BM3D algorithms has been introduced in [30] as a MATLAB Toolbox. Note, that the MATLAB codes for these algorithms are publicly available [30,32].

Here, we use CDBM3D as a generic name of these algorithms. Any of these algorithms can be used in (2).

These algorithms are a generalization for the complex-domain of the popular real-valued Block-Matching 3D filters [33]. Two points define the potential advantage of CDBM3D in comparison, in particular, with using BM3D separately for the phase and amplitude as in [28,34]. Firstly, CDBM3D processes the phase and amplitude jointly taking into consideration the correlation quite usual in most applications, while separate filtering of amplitude and phase ignores this correlation. Secondly, the basis functions in BM3D are fixed, while in CDBM3D they are varying data-adaptive making estimation more precise.

Both types of algorithms BM3D and CDBM3D are based on the non-local similarity of small patches in slice-images always existing in real-life $U_\Lambda(x, y)$. The algorithms look for similar patches in slices $Z(x, y, \lambda)$, identify them and process together. This similarity concept allows to use the powerful modern tools of sparse approximation allowing to design effective denoising algorithms.

The CDBM3D algorithms have a generic structure shown in Fig. 1 and composed from two successive stages: 'thresholding' and 'Wiener filtering'. Each of these stages includes: grouping, 3D/4D High-Order Singular Value Decomposition (HOSVD) analysis, thresholding of HOSVD transforms and aggregation. In the 'Wiener filtering' stage, the thresholding is replaced by Wiener filtering.

Following the procedure in patch-based image processing, the noisy image $Z(x, y, \lambda) \subset \mathbb{C}^{N \times M}$ taken with a fixed λ is partitioned into small overlapping rectangular/squares $N_1 \times M_1$ produced for each pixel of the image. For each patch, we search in $Z(x, y, \lambda)$ for similar patches, identify them and stack them together in 3D groups (array, tensors). This procedure is called grouping, it is the first step of the algorithm shown in Fig. 1.

It follows by HOSVD of these groups defining data-adaptive orthonormal transforms of the complex-valued groups and the core tensors giving the spectral representation of the grouped data.

The next step of the algorithm, as shown in Fig. 1, is filtering implemented as thresholding (zeroing for hard-thresholding) of small items of the core tensors. Inverse HOSVD using the thresholded core tensors returns block-wise estimates of the denoised images. These estimates are aggregated in order to obtain improved image estimates calculated as weighted group-wise estimates. These grouping, HOSVD, thresholding,
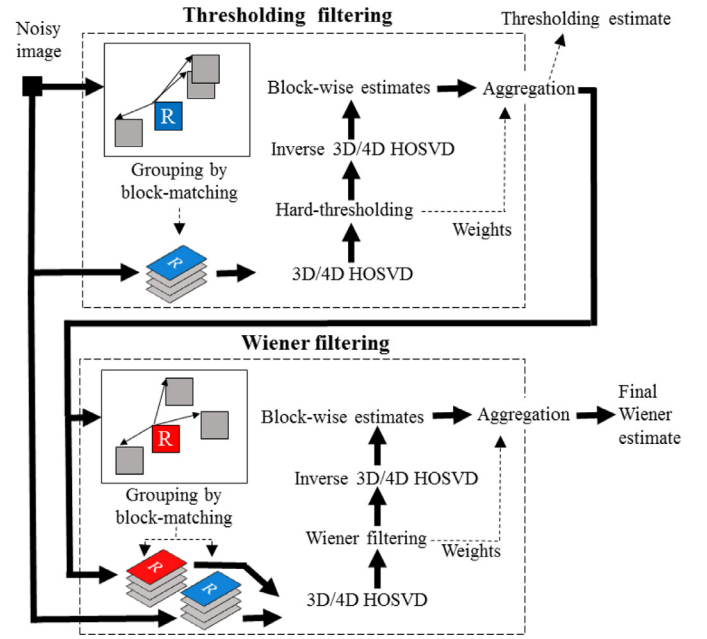

Fig. 1. Flow chart of complex domain CDBM3D filters.

and aggregation define the so-called thresholding filtering, i.e. the first stage of the algorithm in Fig. 1.

The image filtered by thresholding is an input signal of the second stage of the CDBM3D algorithm - Wiener filtering. The structure of this second part of the algorithm is similar to the first thresholding part with the only difference that the thresholding is replaced by the Wiener filtering.

The output of the Wiener filter is the final output of the CDBM3D algorithm. The details of the threshold and Wiener filtering can be seen in [30,32,35]. It is demonstrated in [32,35] that the HOSVD analysis can be produced using instead of complex-valued variables the pairs amplitude/phase or real/imaginary values. Then, the groups become 4D and 4D HOSVD is used for spectral analysis and filtering. The flow chart in Fig. 1 presents a structure valid for both types of the algorithms where we show 3D and 4D HOSVD transforms, respectively.

3.2. Joint slice denoising

Let us introduce a novel algorithm developed especially for joint processing of slices in HS cubes. We use it with the following notations:

$$\hat{U}_{\bar{\Lambda}}(x, y) = CCF\{Z_{\bar{\Lambda}}(x, y), \ \bar{\Lambda} \subset \Lambda\}. \tag{3}$$

Here, $\bar{\Lambda}$ is a set of slices to be denoised. In particular, for sliding filtering considered later in subsection C, $\bar{\Lambda}$ can be defined as symmetric wavelength interval centered at $\lambda = \lambda_0$ of the width δ_{λ_0} :

$$\bar{\Lambda} = \{\lambda : \ \lambda_0 - \delta_{\lambda_0}/2 \le \lambda \le \lambda_0 + \delta_{\lambda_0}/2\}. \tag{4}$$

Complex domain Cube Filter (CCF) processes the data of the cube $Z_{\bar{\Lambda}}(x, y)$ jointly and provide the estimates $\hat{U}_{\bar{\Lambda}}(x, y)$ for all $\lambda \in \bar{\Lambda}$.

The CCF algorithm is presented in Fig. 2 and composed from the following steps.

- Preliminary reshape of 3D data cube $Z_{\bar{\Lambda}}$, $N \times M \times L_{\bar{\Lambda}}$, into the 2D matrix Z of size $L_{\bar{\Lambda}} \times NM$: $N \times M \times L_{\bar{\Lambda}} \rightarrow L_{\bar{\Lambda}} \times NM$;

1. Calculate the orthonormal transform matrix $E \subset \mathbb{C}^{L_{\bar{\Lambda}} \times p}$ and the 2D transform domain eigenimage $Z_{2,eigen}$ as

$$[E, Z_{2,eigen}, p] = HySime(Z), \tag{5}$$

where $HySime$ stays for Hyperspectral signal Subspace Identification by Minimum Error [31], p is a length of the eigenspace.
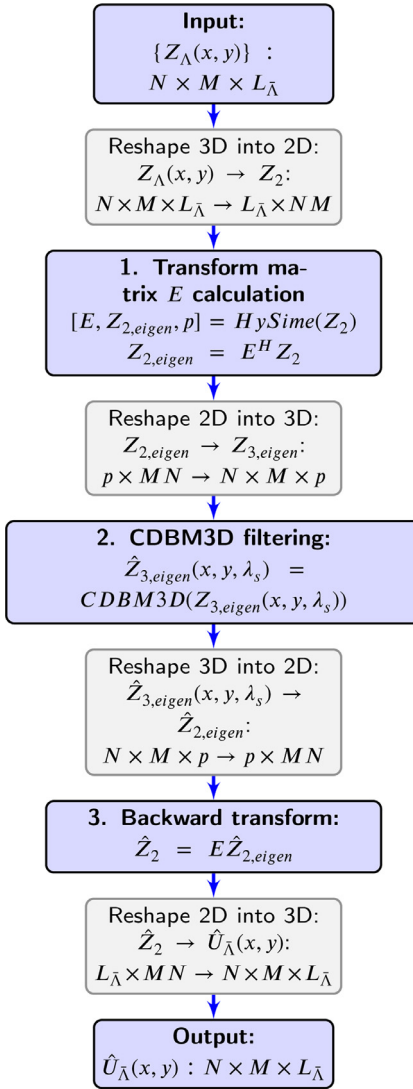
Input:
$$\{Z_\Lambda(x,y)\}:$$
$$N \times M \times L_{\bar\Lambda}$$

Reshape 3D into 2D:
$$Z_\Lambda(x,y) \rightarrow Z_2:$$
$$N \times M \times L_{\bar\Lambda} \rightarrow L_{\bar\Lambda} \times NM$$

1. Transform matrix E calculation
$$[E, Z_{2,eigen}, p] = HySime(Z_2)$$
$$Z_{2,eigen} = E^H Z_2$$

Reshape 2D into 3D:
$$Z_{2,eigen} \rightarrow Z_{3,eigen}:$$
$$p \times MN \rightarrow N \times M \times p$$

2. CDBM3D filtering:
$$\hat{Z}_{3,eigen}(x,y,\lambda_s) = CDBM3D(Z_{3,eigen}(x,y,\lambda_s))$$

Reshape 3D into 2D:
$$\hat{Z}_{3,eigen}(x,y,\lambda_s) \rightarrow \hat{Z}_{2,eigen}:$$
$$N \times M \times p \rightarrow p \times MN$$

3. Backward transform:
$$\hat{Z}_2 = E\hat{Z}_{2,eigen}$$

Reshape 2D into 3D:
$$\hat{Z}_2 \rightarrow \hat{U}_{\bar\Lambda}(x,y):$$
$$L_{\bar\Lambda} \times MN \rightarrow N \times M \times L_{\bar\Lambda}$$

Output:
$$\hat{U}_{\bar\Lambda}(x,y): N \times M \times L_{\bar\Lambda}$$

Fig. 2. $CC\mathcal{F}$ algorithm. Blue blocks are main steps of the algorithm. Gray blocks are technical steps for data arrays 2D⇆3D reshaping.

HySime is an important part of the $CC\mathcal{F}$ algorithm. It identifies an optimal subspace for the HS image representation including both the dimension of the eigenspace p and eigenvectors - columns of E. This algorithm is based on the assumption that the slices $U(x, y, \lambda)$ for $\lambda \subset \Lambda$ are realizations of a random field.

When E is given, the eigenimage is calculated as

$$Z_{2,eigen} = E^H Z. \tag{6}$$

- Reshape the 2D transform domain $Z_{2,eigen}$, $p \times MN$ into the 3D image domain array $Z_{3,eigen}$ of size $N \times M \times p : p \times NM \rightarrow N \times M \times p$;

2. Filter each of the $N \times M$ 2D images (slices) of $Z_{3,eigen}$ by CDBM3D:

$$\hat{Z}_{3,eigen}(x,y,\lambda_s) = \text{CDBM3D}(Z_{3,eigen}(x,y,\lambda_s)). \tag{7}$$

where p eigenvalues λ_s belong to the eigenspace.

- Reshape the 3D array $\hat{Z}_{3,eigen}(x,y,\lambda_s)$ into the 2D transform domain $\hat{Z}_{2,eigen}$ of size $p \times NM$.

3. Return from the eigenimages of the transform domain to the 2D original image space as follows

$$\hat{Z}_2 = E\hat{Z}_{2,eigen}. \tag{8}$$

It is the inverse of the transform of Eq. (6).

- Reshape the 2D image $\hat{Z}_2$ to cube size $N \times M \times L_{\bar\Lambda}$, it gives the resulting filtered cube $\hat{U}_{\bar\Lambda}(x,y)$ (3).

These forward and backward reshape passages 2D⇆3D allow to define the eigenspace $Z_{2,eigen}$ in the 2D transform domain and to produce the CDBM3D filtering in the corresponding 3D domain $Z_{3,eigen}$ slice-by-slice. However, in order to return these filtered data $\hat{Z}_{3,eigen}$ into the original image space we need to use 2D transform (8) and, thus again to reshape 3D data into 2D transform space.

HySime, SVD based algorithm, solves the following problems: estimation of noise and noise covariance matrix and optimization of the signal subspace minimizing mean squared error between the clean HS $U_{\bar\Lambda}(x,y)$ and its estimate. Note, that the covariance $r_{\lambda,\lambda'}(x,y)$ averaged over (x, y) and the preliminary estimate of HS images (not the final (8)) are used in this algorithm. Optimization of the subspace results in minimization of its size and usually the found subspace dimension $p \ll L_{\bar\Lambda}$. It simplifies the processing of HS data and leads to a faster algorithm. Thus, the CDBM3D filtering is produced only for p eigenimages but the backward transform (8) gives the estimates for all $L_{\bar\Lambda}$ spectral images.

The HySime algorithm is a complex domain modification of the HySime algorithm developed for real-valued observations in [36]. More facts concerning the justification of this algorithm as well as motivation and details can be seen in [36] because they are nearly identical to those for the complex domain version of the algorithm.

Overall, the presented $CC\mathcal{F}$ algorithm follows the structure of the fast hyperspectral denoising (FastHyDe) algorithm presented for real-valued data in [31]. A generalization to the complex domain required modification of the codes as well as revision of the theoretical background.

In this paper as the CDBM3D algorithm for eigenimage filtering, we use the ImRe-BM3D WI algorithm [30]. It means that imaginary and real parts of the complex-valued images are used in 4D HOSVD analyses of the 3D grouped data. The algorithm includes both stages: thresholding and Wiener filtering (WI in the algorithm abbreviation). This algorithm enables more efficient performance as compared with the original version of CDBM3D from Katkovnik and Egiazarian [32], where 3D HOSVD is applied to complex-valued images and only thresholding stage is used.

3.3. Sliding window CCF

Statistical modeling and tests of the algorithm show that the reconstructions $\hat{U}(x,y,\lambda_s)$ have the accuracy varying with λ_s and the best results are achieved for λ_s close to the middle point of the interval $\bar\Lambda$. Sliding $CC\mathcal{F}$ is $CC\mathcal{F}$ applied in the sliding mode with the estimate at the step 3 calculated only for $\lambda_s = \lambda_0$ in (4), where λ_0 takes values from Λ. The width of the sliding window $L_{\bar\Lambda}$ can be varying with λ_0.

We make publicly available the MATLAB demo-code of the developed $CC\mathcal{F}$ algorithm, see Code 1.

4. Simulations

4.1. Parameters selection

Simulation experiments are produced for the complex-valued HS cube of a transparent phase object. That means that the amplitude A(x,y) of the object wavefront is equal to 1, and the phase is described by the equation:

$$\varphi_\lambda(x,y) = 2\pi \frac{h(x,y)}{\lambda}(n_\lambda - 1), \tag{9}$$

where λ is a wavelength of radiation going through the object, n_λ is the refractive index of object material and $h(x, y)$ is the thickness of the object.

We model the HS cube for this object by $L_\Lambda = 200$ slices uniformly covering the wavelength interval $\Lambda = 400 \div 798$ nm. The refractive index n_λ is calculated for each λ according to Cauchy's equation with coefficients taken for the glass BK7 [37]. Therefore the noiseless HS cube is represented as $Q_\Lambda(x,y) = \{U(x,y,\lambda), \lambda \subset \Lambda\}$, where $U(x,y,\lambda)=$
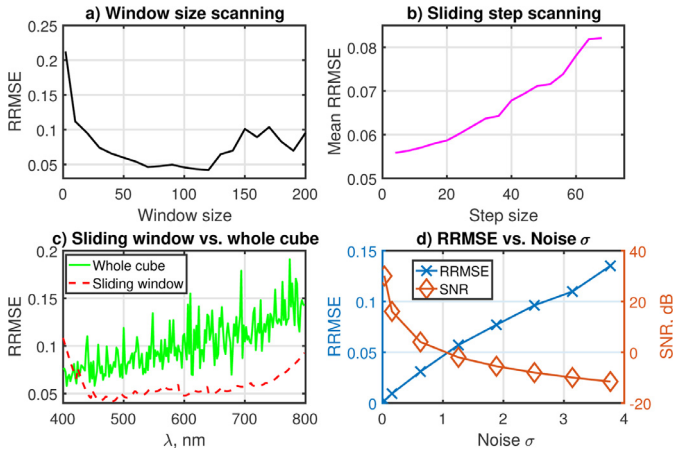
Fig. 3. Phase RRMSE curves. (a) RRMSE dependence on window size $L_{\bar{\lambda}}$; (b) Whole HS cube mean RRMSE dependence on the sliding step; (c) Comparison of RRMSE distributions for filtering by whole HS cube and by sliding window; (d) RRMSE (blue crosses) and SNR (orange diamonds) curves dependence on noise standard deviation σ.

$$= A(x, y) \cdot \exp\left(j\varphi_\lambda(x, y)\right).$$

For noise modeling in the HS cube $Z_\Lambda(x, y)$ (1), we assume that the additive noise ε_Λ is independent and identically distributed complex-valued circular Gaussian with the standard deviation σ.

We use the $CC\mathcal{F}$ algorithm in the sliding window mode (Subsection C). In order to select the proper window size δ_{λ_0}, we produced experiments for the object with the two-peak phase as described in Section 4.2.1. The height of these peaks is selected as small in order the phase variations do not exceed the wrapping range of $[-\pi, \pi)$ for all slices of the HS cube.

The accuracy of phase reconstruction by $CC\mathcal{F}$ is defined as the relative root-mean-squared-error (RRMSE):

$$RRMSE_\varphi = \frac{\sqrt{||\hat{\varphi}_{est} - \varphi_{true}||_2^2}}{\sqrt{||\varphi_{true}||_2^2}}, \tag{10}$$

where $\hat{\varphi}_{est}$ is a reconstructed phase and φ_{true} is a noiseless phase.

The RRMSE curves shown in Fig. 3 illustrate our analysis. The RRMSE curve in Fig. 3(a) is obtained for $\lambda_0 = 598$ nm and calculated for different window size $L_{\bar{\lambda}}$.

The best accuracy is achieved for $L_{\bar{\lambda}}$ somewhere in the interval from 70 to 120. For larger values of $L_{\bar{\lambda}}$, RRMSE is growing what says that estimation is degrading. Such RRMSE behavior is due to that initially with growing windows the algorithm takes into account more slices of HS cube, which are similar to the slice of interest λ_0, therefore it is beneficial for noise suppression and RRMSE curve goes down. However, if the window is too large the slices of the HS cube become too different from the slice of interest λ_0 and, therefore, are not able to improve the estimation and may even corrupt the resulting filtering.

Let we take $L_{\bar{\lambda}} = 70$ as an optimal window size. According to the idea of the sliding window estimation, the algorithm calculations should be repeated for each slice with this fixed window size. However, the neighboring slices have close values of the wavefronts and the $CC\mathcal{F}$ algorithm with the fixed window size and targeted on λ_0 can be used in order to calculate the reconstructions also for neighboring slices. Remind, that this algorithm can give reconstructions for all slices simultaneously. In the sliding window mode of this algorithm, we just select a part from this set of the whole estimates.

In this way, we can obtain much a faster algorithm for wave field reconstruction using $CC\mathcal{F}$ with the sliding window in a step-wise manner, assuming the targeted wavelength λ_0 is changing step-wise with some step-size and the estimates for intermediate slices are filled by the $CC\mathcal{F}$ reconstruction as reminded above.

Fig. 3 (b) shows RRMSE values calculated as the sample mean of RRMSEs for all slices of the HS cube provided the variable step-size for λ_0. It is an almost linear dependence, with a bit flatter behavior for small values of the step-size. The smallest step-size equal to 1 corresponds to the smallest mean RRMSE value, and as a drawback it requires 200 applications of $CC\mathcal{F}$ to cover all slices of the HS cube. As a reasonable trade-off, we took the step-size equal to 12 which corresponds to mean RRMSE smaller than 0.06 but significantly decreases the application number of $CC\mathcal{F}$ from 200 to 17.

Fig. 3 (c) demonstrates a comparison of RRMSE curves for the sliding window step-wise $CC\mathcal{F}$ algorithm with the step-wise equal to 12 (red dotted line) versus a single run of $CC\mathcal{F}$ (green solid line). The advantage of the sliding window technique is obvious with drastically smaller RRMSE values nearly for the whole wavelength interval. Higher values of RRMSE at the lower and upper bounds of the HS cube can be explained by a non-symmetrical neighborhood for the slice of interest.

Fig. 3 (d) illustrates the robustness of the $CC\mathcal{F}$ algorithm regarding the noise level. RRMSEs are mainly smaller than 0.1, corresponding to an acceptable quality of filtering. These results are achieved for very low SNR values, down to -8 dB at $\sigma = 2.5$.

4.2. Comparison with alternative filtering techniques

To demonstrate the advantages of the proposed $CC\mathcal{F}$ algorithm we compare filtering results by different state-of-the-art noise suppression methods and $CC\mathcal{F}$ algorithm for different phase objects. These techniques are: *averaging* [27], BM3D [33], and CDBM3D as in [30].

Averaging technique calculates the mean value of the thickness $h(x, y)$, which should be the same for each slide of the HS cube, after averaging $h(x, y)$ the phases are calculated back (9) for comparison. Since this technique uses the equality of thickness for the whole cube, it can work only for nonwrapped phases, or otherwise, averaging is produced for a small number of neighboring slices. Additionally to account for wavelength-dependent dispersion effect *averaging* technique needs the knowledge of dispersion of object's refractive index [22], which is not always possible.

The comparison tests are carried out for objects of the 3 types of phase: "*interferometric* simple", "*interferometric* compound", and "*wrapped*". HS cube for each case is realized by varying the thickness $h(x, y)$ function of the object. The "*interferometric*" assumes that the phase belongs to the interval $[-\pi, \pi)$. "*Interferometric* simple" means that $h(x, y)$ is a smooth function of (x, y) taken such that for whole set of the wavelengths Λ objects' phases do not exceed the range $[-\pi, \pi)$.

"*Interferometric* compound" is a much more complex model. It corresponds to possible non-smooth rapid variations of the thickness $h(x, y)$, which is composed of a few smooth sections with the "*interferometric*" phases as in the previous case. However, these sections can be completely different. In our tests, we assume that there are three this kind of sections.

This simulation corresponds to objects with different spectral responses in Λ. It is an extreme case for spectral analysis since in real-life such sharp variations of the phase are rare. However, it is an interesting test-image to validate the performance of the algorithms.

"*Wrapped*" means that the phase (absolute phase) corresponding to $h(x, y)$ may take values beyond the interval $[-\pi, \pi)$ and the algorithm reconstructs the wrapped version of this phase. It is a difficult object for filtering as phases can be very different from slice to slice.

For each object, the noisy HS cube is modeled with the noise standard deviation $\sigma = 1.3$.

4.2.1. Interferometric phase simple object

A first investigated object is modeled with a two-peaks Gaussian phase and an invariant amplitude. The clean phase of the slice corresponding to $\lambda = 598$ nm is shown in Fig. 4(a). The corresponding noisy phase of that slice is shown in Fig. 4(b) and results obtained by *averaging*, BM3D, CDBM3D, and $CC\mathcal{F}$ are in Figs. 4(c–f), respectively. It is
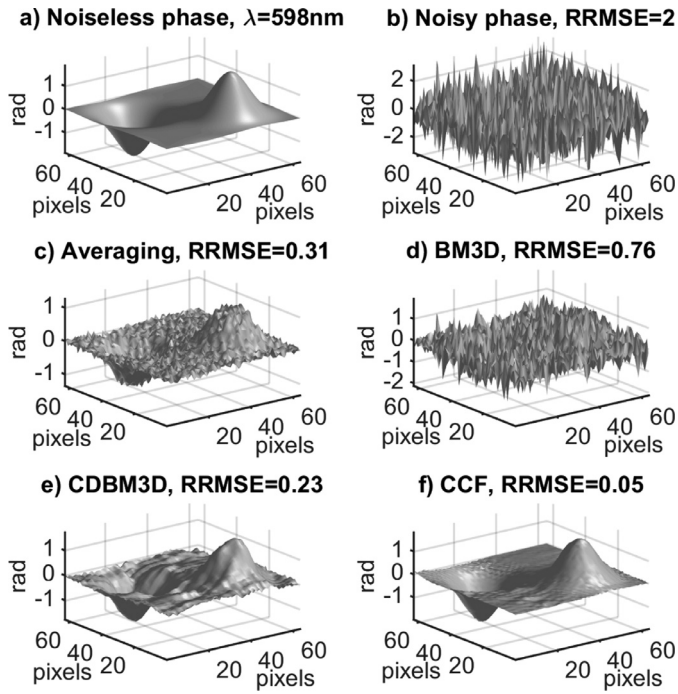
Fig. 4. Objects' and filtered phases not exceeding the range $[-\pi, \pi]$ for slice $\lambda = 598$ nm of the sample with corresponding RRMSE values. (a) Noiseless object phase and (b) with additive noise $\sigma = 1.3$; and phases filtered by: *averaging* (c), BM3D (d), CDBM3D (e), and CCF (f). Filtering results for the whole HS cube see in Visualization 1.
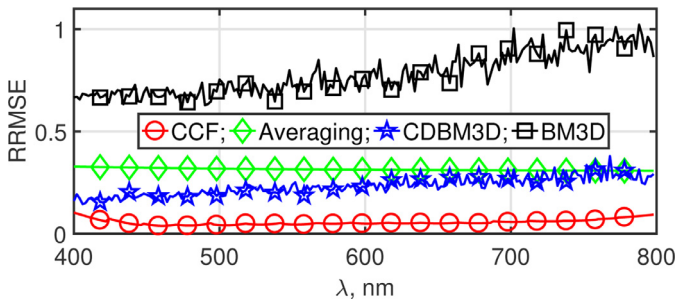

Fig. 5. RRMSE distributions for compared filtering algorithms for the object with non-wrapped phase: red circles curve is for CCF, green diamonds curve is for *averaging*, blue stars is for CDBM3D, black squares curve is for BM3D.

seen from Fig. 4(b) that the noise level is high, and it is just impossible to trace phase variations behind this noise. A significant noise suppression is demonstrated by the *averaging* algorithm in Fig. 4(c), where the averaging is produced over all slices of the HS cube. The method works in this test as the phase for all slices is interferometric and as a result, is of a small range of variation in the cube.

The BM3D algorithm, Fig. 4(d), fails as it is not able to find similar patches for block-matching in the noisy phase slice shown in Fig. 4(b). Better filtering is demonstrated by CDBM3D in Fig. 4(e) due to the joint processing of phase and amplitude. Nevertheless, the corresponding RRMSE value is high, the quality of imaging and the accuracy are not acceptable.

In Fig. 4(f), the result for CCF algorithm is shown. It is seen that noise is suppressed and details of the objects' phase are revealed. The video of these filtering results for all cube's slices is available in Visualization 1.

Fig. 5 presents RRMSEs for the whole HS cube for each of the compared algorithms. The CCF algorithm demonstrates the best accuracy with the RRMSE values smallest for all slices (wavelengths).
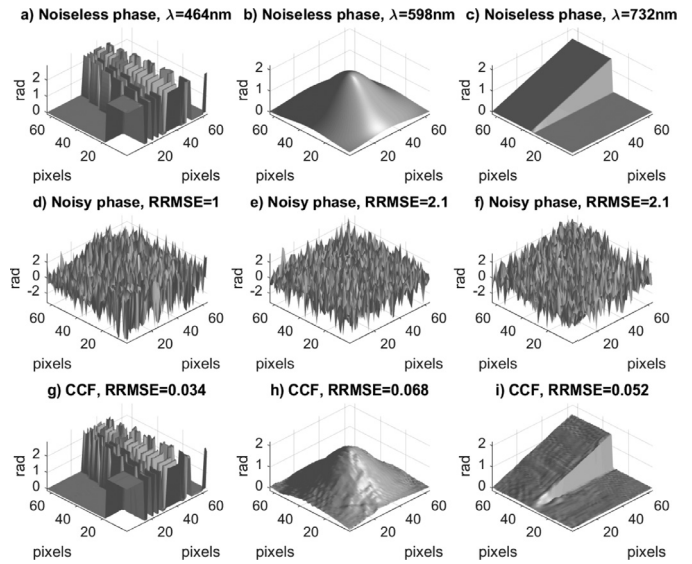

Fig. 6. Compound object phases. Noiseless: (a) slice $\lambda = 464$ nm is USAF target, (b) slice $\lambda = 598$ nm is gaussian peak, (c) $\lambda = 732$ nm is inclined surface; images (d,e,f) are corresponding noisy phases with noise standard deviation $\sigma = 1.3$; and (g,h,i) are filtered phases by CCF of corresponding noisy phases. Filtering results for the whole HS cube see in Visualization 2.
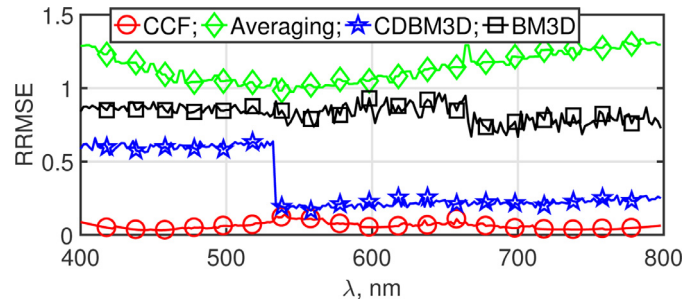

Fig. 7. RRMSE distributions for compared filtering algorithms for non-wrapped compound phase object: red circles curve is for CCF, green diamonds curve is for *averaging*, blue stars is for CDBM3D, black squares curve is for BM3D.

### 4.2.2. Interferometric phase compound object

The second considered phase object was composed from three parts with thicknesses $h(x, y, \lambda_s)$ defined as follows: for $\{\lambda_s, s = [1 \div \frac{1}{3} L_\Lambda)\}$, $h(x, y)$ is a binary USAF test target; for $\{\lambda_s, s = [\frac{1}{3} L_\Lambda \div \frac{2}{3} L_\Lambda)\}$ it is a Gaussian peak, and for $\{\lambda_s, s = [\frac{2}{3} L_\Lambda \div L_\Lambda]\}$ it is an inclined discontinuous surface. The corresponding three parts of the phase slices are shown in Fig. 6(a–c) as noiseless clean and with the high-level additive noise in Fig. 6(d–f).

After filtering by the CCF algorithm working in the sliding window mode, we obtain results shown in Fig. 6(g–i) for each part of the compound phase corresponding to the noisy images in Fig. 6(d–f).

Comparing the filtered phases with the clean images in Fig. 6(a–c) we may conclude that the algorithm enables a high-quality reconstruction working with compound data successfully separating three completely different phase distributions. The demo-video showing results for all wavelength, i.e. for the whole HS cube, is available in Visualization 2.

The RRMSE curves as functions of wavelength are shown in Fig. 7 for the four compared algorithms. The *averaging* algorithm (green diamonds curve) fails completely because the phase images are very different for different parts of the phase object.

CDBM3D and BM3D show different accuracy for different parts of the compound data. In particular, CDBM3D shows a better performance
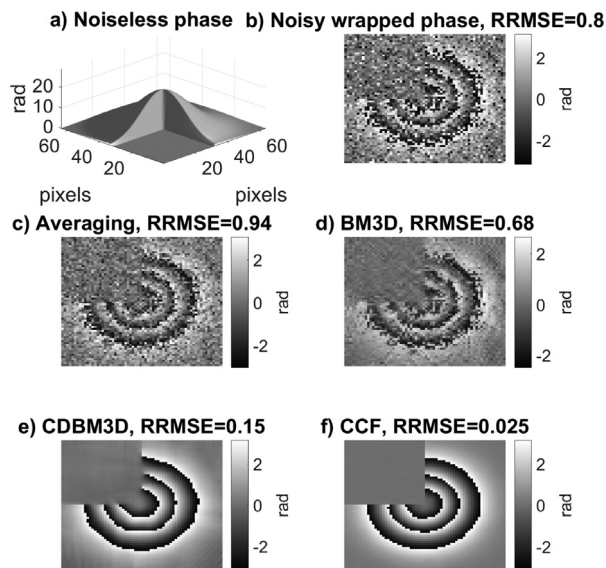
Fig. 8. Objects' and filtered phases for slice $\lambda = 598$ nm of wrapped object with corresponding RRMSE values. Noiseless absolute (a) and noisy ($\sigma = 1.3$) wrapped (b) object phases; and noisy wrapped phases filtered by: *averaging* (c), BM3D (d), CDBM3D (e), and CCF (f). Filtering results for the whole HS cube see in Visualization 3.

for the parts with plain surfaces: Gaussian peak and inclined surface shaped phase.

The CCF curve (red circles) demonstrates the best performance with the smallest RRMSE value more or less invariant with respect to wavelength. Thus, it enables the uniform accuracy for all wavelength despite a great difference between the phase images for different parts of the wavelength interval.

4.2.3. Wrapped phase object

Consider the phase object provided the phase defined by the truncated Gaussian peak with a maximum phase delay $\varphi_{400nm} = 28.9$ rad achieved for $\lambda = 400$ nm. Fig. 8(a) shows the shape of the absolute phase corresponding to the middle slice of the HS cube with $\lambda = 598$ nm.

As the phase takes values out of the interval $[-\pi, \pi]$ the observations are defined by not absolute but wrapped phases. We use the tested algorithms for the reconstruction of these wrapped phases, which are essentially varying on the wavelength range.

The wrapped noisy phase with $\sigma = 1.3$ is presented in Fig. 8(b). The filtering results given by the *averaging*, BM3D, CDBM3D, and CCF algorithms are shown in Figs. 8(c–f), respectively.

The *averaging* algorithm is implemented using a sliding window estimator averaging with the window size equal to 2, i.e. averaging is produced for the pairs of two neighboring slides. The noisy image in Fig. 8(c) and high value of RRMSE indicates that the algorithm fails.

The BM3D algorithm also demonstrates poor visual performance and poor accuracy. CDBM3D produces a much better visual wrapped phase reconstruction but with quite high RRMSE value, thus the accuracy of the wrapped phase reconstruction is not good, Fig. 8(e). CCF algorithm demonstrates the best performance visually and numerically, Fig. 8(f).

The RRMSE curves for the whole HS cube with comparison of the algorithms see Fig. 9 prove the great advantage of the CCF algorithm.

Demo-video showing the results for all algorithms as well as variation of the object phase over the whole wavelength range can be seen Visualization 3.
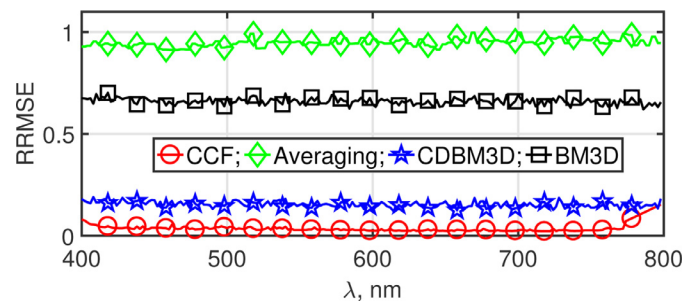
Fig. 9. RRMSE distributions for compared filtering algorithms for wrapped phase object: red circles curve is for CCF, green diamonds curve is for averaging, blue stars is for CDBM3D, black squares curve is for BM3D.
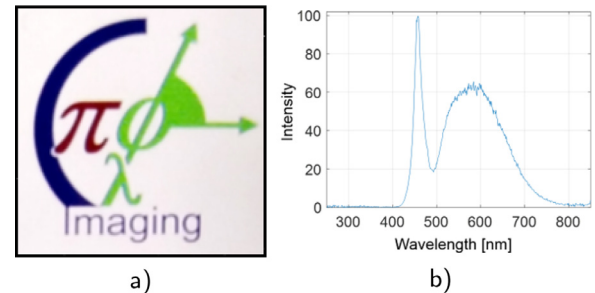
Fig. 10. Transparent object slide 5 mm × 5 mm (a) and used LED spectrum (b).

5. Experimental results

5.1. Object and observed data

The experimental HS data are obtained via spectrally resolved digital holography, as described in [14]. The object is a transparent color slide (Fig. 10(a)) and the light source is a white LED the spectrum of which is shown in Fig. 10(b). In spectral regions of low light intensity, the SNR of the holograms is low and the corresponding reconstructed wavefronts would be more noisy, and in regions where LED intensity is higher, the SNR is higher also and therefore reconstructed wavefronts could be less noisy.

Examples of amplitudes and phases slices of the observed HS data are shown in the top rows of Figs. 11 and 12 for amplitudes and phases corresponding to 503 nm (less noisy) and 743 nm (more noisy), respectively. For the less noisy 503 nm slice (top row Fig. 11), the structure of the object is clearly seen in both phase and amplitude, while for the noisier slice 743 nm (top row Fig. 12) it is hard to distinguish details of the object behind noise.

### 5.2. Results of data processing

The noise level is sufficiently suppressed in the whole HS cube after the CCF filtering. Object details are revealed for every slice regardless of the noise level, see bottom rows in Figs. 11 and 12. Video-demo with the filtering results for the whole HS cube are presented in Visualization 4.

Furthermore, the CCF filter enables the recovery of information that was nearly completely lost in the observed noisy slices. For a demonstration of the correctness of the CCF filtering, we compare three slices: 1) the slice 446 nm from noisy non-filtered HS cube with 2) the same noisy slice from the HS cube but filtered by CCF and 3) the non-filtered 446 nm slice obtained for the same test-object, in the same optical setup but in another experiment with much higher SNR.

In this way, we compare the results of our denoising with experimental data obtained for the identical optical scenario but with much higher exposure time, i.e. lower noise level. This comparison is of importance in order to test our reconstructions on correctness versus possible arti-
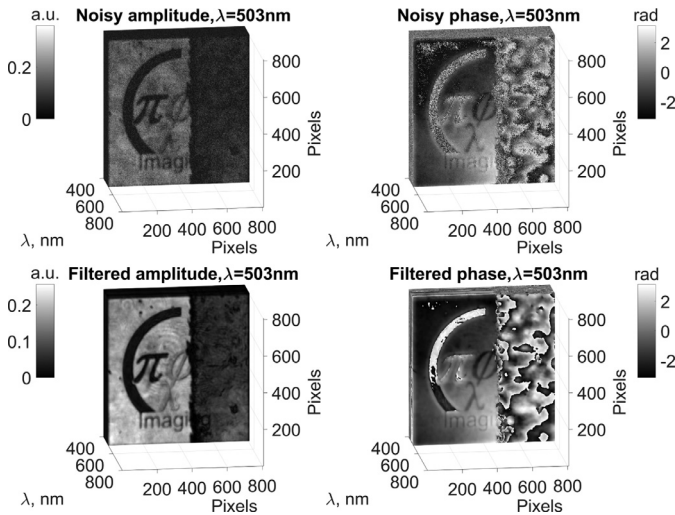
Fig. 11. Images of objects' amplitude and phase corresponding to $\lambda = 503$ nm slice of the HS cube. Top row: noisy amplitude (left) and phase (right); bottom row: CCF filtered amplitude and phase, correspondingly. Filtering results for the whole HS cube see in Visualization 4.
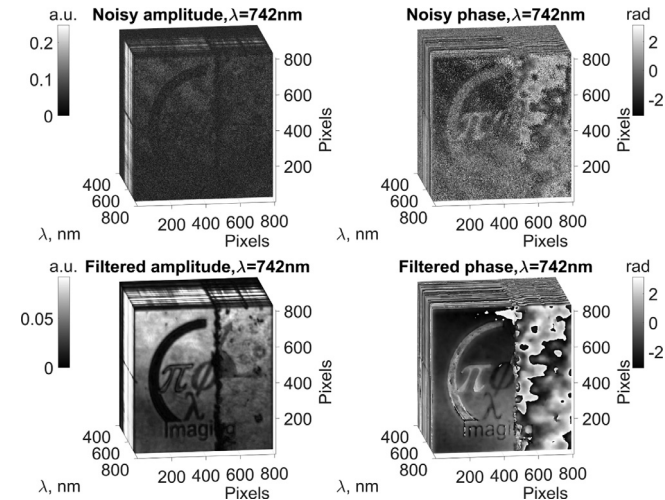

Fig. 12. Images of objects' amplitude and phase corresponding to $\lambda = 742$ nm slice of the HS cube. Top row: noisy amplitude (left) and phase (right); bottom row: CCF filtered amplitude and phase, correspondingly. Filtering results for the whole HS cube see in Visualization 4.

facts which can appear in the tested slice from other slices of the HS cube.

In Fig. 13, the top row is for amplitudes and the bottom row is for phases; from left to right: the first column is for images of noisy slice, the second column is for CCF filtered, the third one is for the noisy slice of the higher SNR. In the fourth column, we show the cross-sections of the images shown in the columns 1–3.

We can see, that the information almost completely lost in the noisy slice (Fig. 13(a,e)) is revealed by the CCF algorithm (Fig. 13(b,f)) and these found amplitude/phase features coincide with those clearly seen in the slice of higher SNR (Fig. 13(c,g)).

The amplitude cross-sections that are presented in Fig. 13(d) are normalized/scaled to the interval [0,1], since the HS cubes were obtained with different light intensities in the compared two experiments. Nevertheless, the comparison qualitatively confirms that there are no visual artifacts generated by the algorithm and the obtained filtered amplitude/phase changes correspond to more precise observations obtained from the higher SNR experiment. From the comparison of amplitude
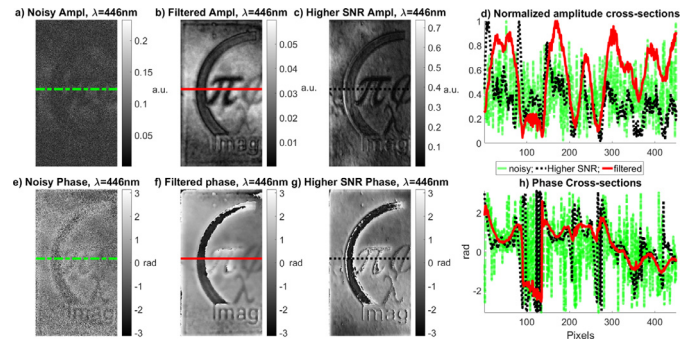
Fig. 13. Comparison of noisy amplitude (a) and phase (e) of slice corresponding to $\lambda = 446$ nm with filtered amplitude (b) and phase (f) by CCF algorithm and with amplitude (c) and phase (g) from HS cube with higher SNR. Longitudinal cross-sections for phases and amplitudes are in (d) and (h), respectively. Green curve is for noisy slice, red is for slice filtered by CCF algorithm, and black is for slice with higher SNR.

Table 1

Noise statistics for real and imaginary parts of the experimental HS cube.

Moment	Real part	Imaginary part
Expectation	$1.2 \cdot 10^{-4}$	$4.6 \cdot 10^{-6}$
Standard deviation	0.0424	0.0424

cross-sections, it can be concluded that for the amplitude filtered by CCF (red solid curve) all object features are revealed in the same locations as in the amplitude of the HS cube with higher SNR (black dotted curve). Different values of the amplitudes in the cross-sections can be referred to different illuminations in the considered two experiments.

The phase cross-sections in Fig. 13(h) also confirm that there are no visual artifacts produced by the algorithm CCF filtering (red solid curve) and the phase curves are quite close to those obtained in the experiment with a higher SNR. The noise level in the CCF curve is even lower than that in the experiment with higher SNR (black dotted curve). In both amplitude and phase cross-sections, the green curves correspond to the noisy observed slice and indicate very noisy data.

5.3. Noise in experimental data

Let us test the validity of the noise model introduced in Eq. (1).

For the noise analysis, we introduce the complex-valued residuals as differences between the noisy complex-valued observations $Z_\Lambda(x, y)$ and reconstructed filtered complex-valued HS cube $\hat{Q}_\Lambda(x, y)$:

$$\varepsilon_\Lambda(x, y) = Z_\Lambda(x, y) - \hat{Q}_\Lambda(x, y). \tag{11}$$

Assuming that our estimation is good enough, we use these residuals as HS cube noise estimates. It is one of the standard approaches to noise estimation in statistics. From these residuals, we calculated expectations, standard deviation, and correlations as well as distributions of real and imaginary parts of the complex-valued noise. In what follows, we are restricted to the global analysis only, when the averaging is produced over all pixels of the HS residual cube.

In Table 1, we can see the mean values, standard deviations for real and imaginary parts of the noise. The correlation coefficient between real and imaginary parts is equal to 0.002, which means that the real and imaginary parts of the noise are completely non-correlated.

Fig. 14 shows the distribution of the real and imaginary parts also calculated over the whole HS cube. The red contours show the Gaussian approximations for these distributions. We may conclude from these results, that indeed the noise is Gaussian complex-valued with independent real and imaginary parts, having identical distributions, which perfectly corresponds to the noise model introduced in Section 2.
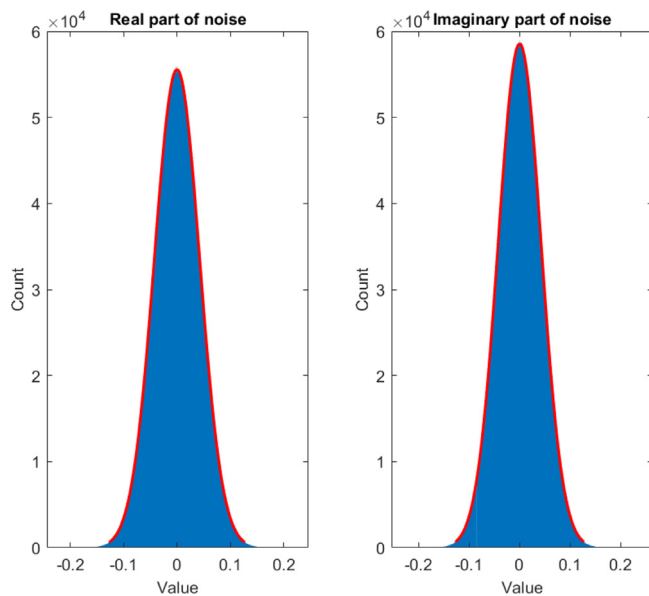
Fig. 14. Histograms for real (left) and imaginary (right) parts of the HS cube of the noise residuals. The red contours show the Gaussian approximations for the distributions.

6. Conclusion

In this paper, we present the denoising algorithm for hyperspectral complex-valued data. Based on comprehensive investigations, we have demonstrated the state-of-the-art performance of the algorithm owing to the SVD analysis of noisy hyperspectral observations and complex domain BM3D filtering in the reduced dimension SVD eigenspace. The study includes multiple simulation tests and processing of those and HS digital holography data. The algorithm is robust with respect to noisy data, and produces reliable results even for extra-low SNR, down to -8 dB. It demonstrates a stable effective performance for different types of HS data with interferometric and wrapped phases, the latter without involving unwrapping procedures.

Traditional filtering techniques for complex-valued HS data perform noise suppression based only on spatial information and do not use the advantage of the third dimension, therefore they fail on cube slices with low SNR, where object information masked by noise. Contrariwise, the proposed CCF algorithm uses the joint processing of all slices of HS data, suppresses noise, and retrieves data that was lost for the whole HS cube, including slices with low SNR. Moreover, traditional techniques fail on phase filtering due to its proneness to wrapping. In CCF the wrapping problem is overcome by CDBM3D which provides noise suppression regardless of phase wrapping.

We believe that the extremely high performance of our technique of processing interferometric data cubes demonstrated in this work will eliminate the key constraint preventing the widespread usage of phase HSDH imaging at practice. In particular, the following areas are attractive for this technique: (i) spatial-spectral analysis of biological products in the visible ultraviolet spectral ranges (as an example, see the work [38]); (ii) HS analysis of dispersion and absorption properties in near-infrared Fourier spectroscopy (see details e.g. in [39]) extended with the addition of spatial degrees of freedom; (iii) Development of new approaches for non-invasive taxonomy of marine plankton based on broadband phase imaging. For such techniques background, see [40]; (iv) Analysis of the broadband wavefront propagation dynamics through the scattering and dispersive media [41].

Declaration of Competing Interest

None.

Supplementary material

Supplementary material associated with this article can be found, in the online version, at 10.1016/j.optlaseng.2019.105973.

References

[1] Tsagkatakis G, Jayapala M, Geelen B, Tsakalides P. Non-negative matrix completion for the enhancement of snapshot mosaic multispectral imagery. Electron Imaging 2016;2016(12):1–6. doi:10.2352/ISSN.2470-1173.2016.12.IMSE-277.

[2] Govender M., Chetty K., Bulcock H.. A review of hyperspectral remote sensing and its application in vegetation and water resource studies. 2007. URL http://www.ajol.info/index.php/wsa/article/view/49049. 10.4314/wsa.v33i2.49049

[3] Chin MS, Chappell AG, Giatsidis G, Perry DJ, Lujan-Hernandez J, Haddad A, et al. Hyperspectral imaging provides early prediction of random axial flap necrosis in a preclinical model. Plast Reconstr Surg 2017;139(6):1285e–1290e. doi:10.1097/PRS.0000000000003352.

[4] Chapman HN, Nugent KA. Coherent lensless x-ray imaging. Nat Photonics 2010;4(12):833.

[5] Shapiro D, Thibault P, Beetz T, Elser V, Howells M, Jacobsen C, et al. Biological imaging by soft x-ray diffraction microscopy. Proc Natl Acad Sci 2005;102(43):15343–6.

[6] Holler M, Guizar-Sicairos M, Tsai EH, Dinapoli R, Müller E, Bunk O, et al. High-resolution non-destructive three-dimensional imaging of integrated circuits. Nature 2017;543(7645):402.

[7] Dorrer C, Belabas N, Likforman J-P, Joffre M. Spectral resolution and sampling issues in fourier-transform spectral interferometry. JOSA B 2000;17(10):1795–802.

[8] Debnath SK, Kothiyal MP, Schmit J, Hariharan P. Spectrally resolved phase-shifting interferometry of transparent thin films: sensitivity of thickness measurements. Appl Opt 2006;45(34):8636–40.

[9] Kalenkov S, Kalenkov G, Shtanko A. Spectrally-spatial fourier-holography. Opt Express 2013;21(21):24985–90.

[10] Tenner VT, Eikema KS, Witte S. Fourier transform holography with extended references using a coherent ultra-broadband light source. Opt Express 2014;22(21):25397–409.

[11] Eisebitt S, Lüning J, Schlotter W, Lörgen M, Hellwig O, Eberhardt W, et al. Lensless imaging of magnetic nanostructures by x-ray spectro-holography. Nature 2004;432(7019):885.

[12] Sandberg R, Raymondson D, Paul A, Raines K, Miao J, Murnane M, et al. Table-top soft-x-ray fourier transform holography with 50 nm resolution. Opt Lett 2009;34(11):1618–20.

[13] Naik DN, Pedrini G, Takeda M, Osten W. Spectrally resolved incoherent holography: 3D spatial and spectral imaging using a Mach–Zehnder radial-shearing interferometer. Opt Lett 2014;39(7):1857. doi:10.1364/OL.39.001857.

[14] Claus D, Pedrini G, Buchta D, Osten W. Accuracy enhanced and synthetic wavelength adjustable optical metrology via spectrally resolved digital holography. J Opt Soc Am A 2018;35(4):546–52. doi:10.1364/JOSAA.35.000546.

[15] Witte S, Tenner VT, Noom DW, Eikema KS. Lensless diffractive imaging with ultra-broadband table-top sources: from infrared to extreme-ultraviolet wavelengths. Light 2014;3(3):e163.

[16] Jansen G., de Beurs A., Liu X., Eikema K., Witte S.. Diffractive shear interferometry for extreme ultraviolet high-resolution lensless imaging. arXiv 2018; 1802.07630.

[17] Itoh K, Inoue T, Yoshida T, Ichioka Y. Interferometric supermultispectral imaging. Appl Opt 1990;29(11):1625. doi:10.1364/ao.29.001625.

[18] Bell RJ. Introductory fourier transform spectroscopy.. Academic Press; 1972.

[19] Bespalov VG, Gorodetskii AA. Modeling of referenceless holographic recording and reconstruction of images by means of pulsed terahertz radiation. J Opt Technol 2007;74(11):745. doi:10.1364/JOT.74.000745.

[20] Petrov NV, Kulya MS, Tsypkin AN, Bespalov VG, Gorodetsky A. Application of terahertz pulse time-Domain holography for phase imaging. IEEE Trans Terahertz Sci Technol 2016;6(3):464–72. doi:10.1109/TTHZ.2016.2530938.

[21] Holl PM, Reinhard F. Holography of Wi-Fi radiation. Phys Rev Lett 2017;118(18):183901.

[22] Kulya MS, Balbekin NS, Gredyuhina IV, Uspenskaya MV, Nechiporenko AP, Petrov NV. Computational terahertz imaging with dispersive objects. J Mod Opt 2017;64(13):1283–8. doi:10.1080/09500340.2017.1285064.

[23] Katkovnik V, Shevkunov I, Petrov N, Eguiazarian K. Multiwavelength absolute phase retrieval from noisy diffractive patterns: wavelength multiplexing algorithm. Appl Sci 2018;8(5):719–38. doi:10.3390/app8050719.

[24] Katkovnik V, Shevkunov I, Petrov NV, Egiazarian K. Multiwavelength surface contouring from phase-coded noisy diffraction patterns: wavelength-division optical setup. Opt Eng 2018;57(8):1. doi:10.1117/1.OE.57.8.085105.

[25] Feng F, Deng C, Wang W, Dai J, Li Z, Zhao B. Constrained nonnegative matrix factorization for robust hyperspectral unmixing. In: IGARSS 2018 - 2018 IEEE International geoscience and remote sensing symposium. IEEE; 2018. p. 4221–4. ISBN 978-1-5386-7150-4. doi:10.1109/IGARSS.2018.8517818.

[26] Obara M, Yoshimori K. Systematic study of synthetic aperture processing in interferometric three-dimensional imaging spectrometry. Jpn J Appl Phys 2017;56(2):022402. doi:10.7567/JJAP.56.022402.

[27] Kalenkov SG, Kalenkov GS, Shtanko AE. Hyperspectral holography: an alternative application of the fourier transform spectrometer. J Opt Soc Am B 2017;34(5):B49. doi:10.1364/JOSAB.34.000B49.

[28] Kalenkov GS, Kalenkov SG, Meerovich IG, Shtanko AE, Zaalishvili NY. Hyperspectral holographic microscopy of bio-objects based on a modified linnik interferometer. Laser Phys 2019;29(1):16201. doi:10.1088/1555-6611/aaf228.

[29] Katkovnik V, Shevkunov I, Claus D, Pedrini G, Egiazarian K. Non-local similarity complex domain denoising for hyperspectral phase imaging. OPAL conference. Sensors and Transducers, editor; 2019. Amsterdam

[30] Katkovnik V, Ponomarenko M, Egiazarian K. Sparse approximations in complex domain based on BM3D modeling. Signal Process 2017;141:96–108. doi:10.1016/j.sigpro.2017.05.032.

[31] Zhuang L, Bioucas-Dias JM. Fast hyperspectral image denoising and inpainting based on low-Rank and sparse representations. IEEE J Sel Top Appl Earth Obs Remote Sens 2018;11(3):730–42. doi:10.1109/JSTARS.2018.2796570.

[32] Katkovnik V, Egiazarian K. Sparse phase imaging based on complex domain nonlocal BM3D techniques. Digital Signal Process 2017;63:72–85. doi:10.1016/j.dsp.2017.01.002.

[33] Dabov K, Foi A, Katkovnik V, Egiazarian K. Image denoising by sparse 3-D transform-domain collaborative filtering. IEEE Trans Image Process 2007;16(8):2080–95. doi:10.1109/TIP.2007.901238.

[34] Katkovnik V, Astola J. Phase retrieval via spatial light modulator phase modulation in 4f optical setup: numerical inverse imaging with sparse regularization for phase and amplitude. J Opt Soc Am A 2012;29(1):105. doi:10.1364/JOSAA.29.000105.

[35] Katkovnik V., Ponomarenko M., Egiazarian K.. Complex-valued image denosing based on group-wise complex-domain sparsity. 2017b. URL http://arxiv.org/abs/1711.00362.

[36] Bioucas-Dias JM, Nascimento JM. Hyperspectral subspace identification. IEEE Trans Geosci Remote Sens 2008;46(8):2435–45. doi:10.1109/TGRS.2008.918089.

[37] Hartmann P. Optical glass. SPIE PRESS BOOK; 2014. ISBN 9781628412925.

[38] Soltani S, Ojaghi A, Robles FE. Deep UV dispersion and absorption spectroscopy of biomolecules. Biomed Opt Express 2019;10(2):487. doi:10.1364/BOE.10.000487.

[39] Manley M. Near-infrared spectroscopy and hyperspectral imaging: non-destructive analysis of biological materials. Chem Soc Rev 2014;43(24):8200–14. doi:10.1039/C4CS00062E.

[40] Gorocs Z, Tamamitsu M, Bianco V, Wolf P, Roy S, Shindo K, et al. A deep learning-enabled portable imaging flow cytometer for cost-effective, high-throughput, and label-free analysis of natural water samples. Light Sci Appl 2018;7(1):66. doi:10.1038/s41377-018-0067-0.

[41] Mounaix M, Andreoli D, Defienne H, Volpe G, Katz O, Grésillon S, et al. Spatiotemporal coherent control of light through a multiple scattering medium with the multispectral transmission matrix. Phys Rev Lett 2016;116(25):253901. doi:10.1103/PhysRevLett.116.253901.